Monthly Notices of the ROYAL ASTRONOMICAL SOCIETY
MNRAS Advance Access published July 24, 2013
MNRAS (2013) doi:10.1093/mnras/stt1074

Solar scintillation detection and ranging (SCIDAR) technique for measuring turbulent-layer heights

Noriaki Miura,[1]⋆ Ayumu Oh-ishi,[1] Shingo Shionoya,[1] Koji Watanabe,[1] Susumu Kuwamura,[1] Naoshi Baba,[2] Satoru Ueno[3] and Kiyoshi Ichimoto[3]

[1]*Department of Computer Sciences, Kitami Institute of Technology, 165 Koen-cho, Kitami, Hokkaido 090-8507, Japan*
[2]*Department of Applied Physics, Graduate School of Engineering, Hokkaido University, Sapporo, Hokkaido 060-8628, Japan*
[3]*Hida Observatory, Graduate School of Science, Kyoto University, Kamitakara, Takayama, Gifu 506-1314, Japan*

Accepted 2013 June 12. Received 2013 June 10; in original form 2013 January 19

ABSTRACT

A solar SCIDAR (scintillation detection and ranging) technique is proposed for measuring the heights of turbulent layers using the Sun itself, instead of the binary stars used in night-time SCIDAR. A formula for the technique is derived under various assumptions: uniform intensity distributions on the solar surface and sparse speckle distributions on the image plane. It indicates that the cross-correlation of scintillation shadows yields peaks at positions corresponding to layer heights, although the shapes of peaks are blurred by both an extended seeing disc and a finite-sized field stop. A knife-edge effect caused by field stops in an observational system is also described, which yields another peak at the centre of the correlation plane. Observations were conducted using a solar SCIDAR system developed at the Hida Observatory in Japan. In many results, peaks on correlation planes demonstrated a contrast high enough for them to be distinguished from the background. Most of the distances to turbulent layers derived from the scintillation peaks were found to be between 2.5 and 3.5 km. Use of a high-performance adaptive-optics system upstream of the SCIDAR system is suggested in order to provide better results.

Key words: turbulence – atmospheric effects – instrumentation: adaptive optics – methods: observational – site testing – Sun: general.

1 INTRODUCTION

Adaptive optics (AO) systems are currently being developed for the purposes of solar observations (Rimmele 2000; Langlois et al. 2004; Schmidt et al. 2009). Next-generation solar AO requires multiconjugate (MC) compensation so as to widen the corrected field of view to a size comparable to large active regions on the solar surface. We are developing a solar AO system for the domeless solar telescope of the Hida Observatory in Japan (Miura et al. 2006, 2007; Miura et al. 2009; Miura et al. 2011, 2012), and are planning to improve it to include MC compensation. Information on layer heights with strong turbulence is required when designing an MCAO system.

Several seeing-measurement techniques are available for solar observations (Beckers & Rimmele 2004; Beckers 2001; Beckers et al. 1997; Kawate et al. 2011). In particular, the shadow band ranging technique was successfully applied to the site survey for the Advanced Technology Solar Telescope (Beckers & Mason 1998). The technique enables the measurement of seeing conditions in the vertical direction without a telescope, especially at lower altitudes. For our purpose, however, it is necessary to measure the heights of higher layers.

The scintillation detection and ranging (SCIDAR) technique has been successfully applied to probing atmospheric turbulence at higher altitudes (Rocca, Roddier & Vernin 1974; Beran & Whitman 1988; Avila, Vernin & Masciadri 1997; Klückers et al. 1998; Avila, Vernin & Sánchez 2001; Weiß et al. 2002; Garnier 2007). In night-time SCIDAR observations, binary stars are used as objects, and many pupil images are recorded with short exposure times. If there is a turbulent layer at a given height, two scintillation patterns originating from the two components of a binary star overlap with some shift on the pupil plane. The amount of shift is proportional to both the layer height and the separation of the binary components. The magnitude of the scintillation depends on both the layer height and the strength of the turbulence. The ensemble-averaged autocorrelation of the pupil images yields information on the structure constant of the refractive index fluctuations, $C_n^2(h)$, which characterizes the contribution of atmospheric turbulence for wave propagation through a turbulent layer at a height h. The

⋆ E-mail: miuranr@mail.kitami-it.ac.jp

SCIDAR and similar techniques can also be used to measure the wind velocity in the layers (Klückers et al. 1998; Avila et al. 2001; Horikawa et al. 2004).

Beckers & Rimmele (2004) reported a SCIDAR technique for solar observations. They used a lenslet array, in which small lenses sampled solar surface structures at different positions, and then observed the array of pupil images with different directions of view. Choosing any two of the pupil images corresponds to the simultaneous observation of binary stars with various separations and directions. In their experiments, however, no turbulent layer was detected.

In this paper we propose another type of solar SCIDAR, in which two field stops (FSs) with variable separations are used as a pseudo-binary star. In our system, two pupil images passing through the FSs are simultaneously observed on a detector. Compared with the technique using a lenslet array, the variety of separations and directions for the pupil pair is lost. However, the size of FSs and separation between them are arbitrarily determined in our technique. We present, to our knowledge for the first time, a formula for solar SCIDAR.

Some problems in our solar SCIDAR technique should be noted.

(A) A solar image degraded by atmospheric turbulence is sampled with the two FSs. Therefore, the pupil scintillation patterns observed on the detector must be affected by phase errors on the pupil plane. How is this effect estimated?

(B) The two FSs are regarded as extended objects, while each component of a binary star is a point source. What is changed in SCIDAR when extended objects are used?

(C) The Sun is a widely extended object beyond the size of a FS. Therefore, the FSs play the role of knife edges in the well-known knife-edge test, as indicated by Beckers & Rimmele (2004). How do the knife edges act in our SCIDAR technique?

In Section 2, we briefly review the night-time SCIDAR and present our SCIDAR technique. Section 3 details an observational setup. Section 4 summarizes the results of SCIDAR observations made at the Hida Observatory in 2012 May and June. Sections 5 and 6 contain a discussion and the conclusions, respectively.

2 SCIDAR FOR SOLAR OBSERVATION

2.1 Review of night-time SCIDAR

To describe the optical path fluctuations through an atmosphere with refractive index fluctuations, the small-perturbation approximation is usually used: the phase fluctuation $\phi(\boldsymbol{r})$ caused by a thin layer at height h is very small, where $\boldsymbol{r} = (x, y)$ is the vector of horizontal coordinates. The wavefront propagates to the telescope through a free space, with the propagation described by the Fresnel diffraction formulation, to yield the wavefront $\psi_0(\boldsymbol{r})$ at the aperture. The observed pupil intensity is then $|\psi_0(\boldsymbol{r})|^2$. Its fluctuation, namely scintillation, is defined as

$$F(\boldsymbol{r}) = \frac{|\psi_0(\boldsymbol{r})|^2 - \left\langle |\psi_0(\boldsymbol{r})|^2 \right\rangle}{\left\langle |\psi_0(\boldsymbol{r})|^2 \right\rangle}, \tag{1}$$

where $\langle\,\rangle$ denotes the ensemble average. It is related to $\phi(\boldsymbol{r})$ as

$$F(\boldsymbol{r}) = \phi(\boldsymbol{r}) * \left[\frac{2}{\lambda h}\cos\left(\frac{\pi \boldsymbol{r}^2}{\lambda h}\right)\right], \tag{2}$$

where λ is the wavelength and * denotes the convolution operation. The ensemble-averaged autocorrelation of $F(\boldsymbol{r})$ is known to be (Garnier 2007)

$$B_h(x, y, h) = 3.9 \times 10^{-2} \times 2\pi k^2 C_n^2(h) \int_0^\infty \mathrm{d}\rho\ \rho^{-8/3} \sin^2\left(\pi\lambda h\rho^2\right) J_0(2\pi r\rho), \tag{3}$$

where k is the wavenumber, $r = (x^2 + y^2)^{1/2}$, and J_0 is the zeroth-order Bessel function of the first kind. The formula for a multiple-layer case is obtained by

$$B(x, y) = \int_0^\infty \mathrm{d}h\ B_h(x, y, h). \tag{4}$$

When using a binary star with an angular separation of θ, scintillation patterns from individual binary components are separated by θh on the pupil plane. The ensemble-averaged autocorrelation of such scintillation patterns yields three peaks, at the centre, θh and $-\theta h$. When the binary components align in the x-direction, equation (4) becomes

$$B(x, y) = \int_0^\infty \mathrm{d}h\ \left[\frac{1+\alpha^2}{(1+\alpha)^2} B_h(x, y, h) + \frac{\alpha}{(1+\alpha)^2} B_h(x - \theta h, y, h) + \frac{\alpha}{(1+\alpha)^2} B_h(x + \theta h, y, h)\right], \tag{5}$$

where α is the intensity ratio of the binary components. From the positions and strengths of the side peaks along the x-axis, $C_n^2(h)$ can be derived.

2.2 Scintillation from blurred image

Fig. 1 illustrates an observational situation for our solar SCIDAR. The coordinates on the focal plane are denoted by $\boldsymbol{w} = (u, v)$. Through the same two FSs at the positions $\boldsymbol{w}_a = (u_a, 0)$ and $\boldsymbol{w}_b = (0, 0)$, two pupil images are respectively observed on the detector. The two FSs

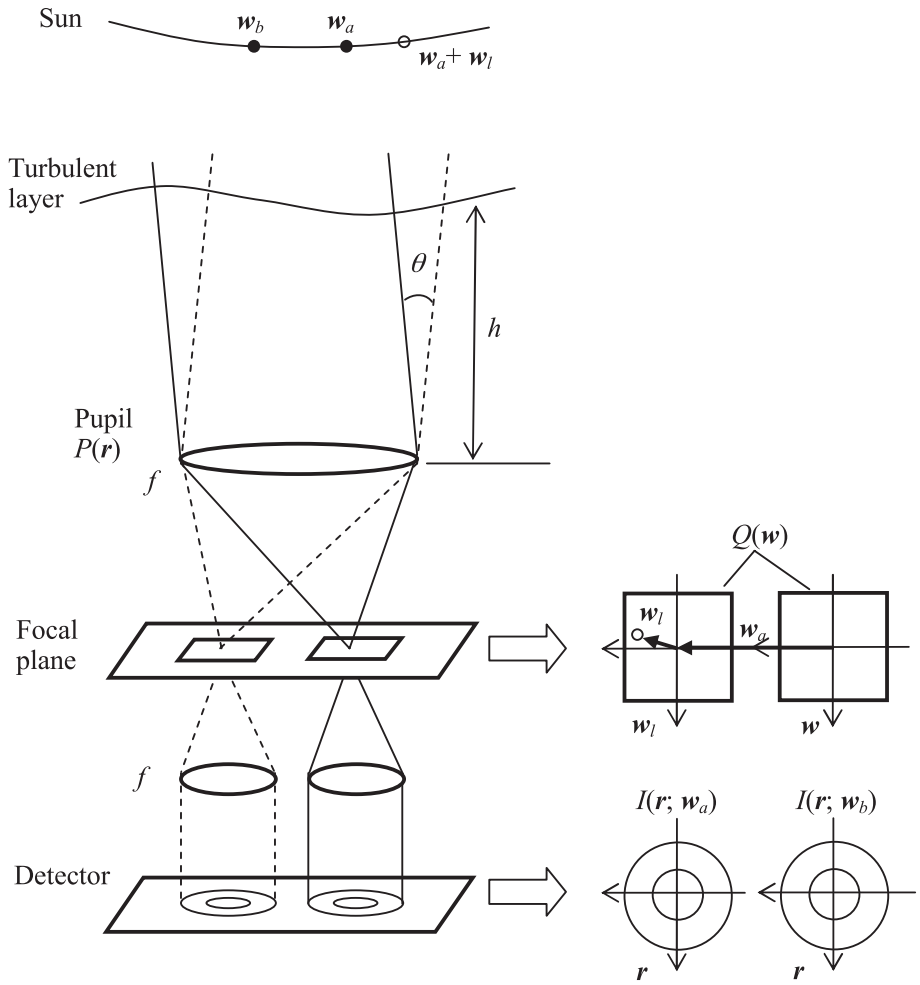

Figure 1. Schematic description of solar SCIDAR observations.

are regarded as a pseudo-binary star with an angular separation of $\theta = u_a f$, where f is the telescope focal length. We assume the Sun to be an incoherent light source with uniform brightness with unit intensity (see Section 5.2). This assumption makes the following formulation simpler.

We model the wavefront on the pupil plane ($h = 0$) coming from the point (0,0) on the solar surface as

$$\psi_0(\boldsymbol{r}) = |\psi_0(\boldsymbol{r})| \exp[\mathrm{i}\phi_0(\boldsymbol{r})] \ . \tag{6}$$

The wavefront passes through the telescope aperture and then becomes, using $s(\boldsymbol{r}) = |\psi_0(\boldsymbol{r})|$ and $t(\boldsymbol{r}) = \exp[\mathrm{i}\phi_0(\boldsymbol{r})]$,

$$\psi_p(\boldsymbol{r}) = s(\boldsymbol{r})\, t(\boldsymbol{r})\, p(\boldsymbol{r}) \tag{7}$$

on the pupil plane, and

$$\Psi_p(\boldsymbol{w}) = S(\boldsymbol{w}) * T(\boldsymbol{w}) * P(\boldsymbol{w}) \tag{8}$$

on the focal plane. The function $p(\boldsymbol{r})$ is unity inside the aperture and zero elsewhere. An uppercase function denotes the Fourier transform of the associated lowercase function.

In speckle interferometry (Labeyrie 1970; Dainty 1975; Roddier 1981), $s(\boldsymbol{r}) = 1$ is assumed, and $|\Psi_p(\boldsymbol{w})|^2$ is regarded as a set of speckles. The size of each speckle is comparable to the Airy disc size. Therefore, such a speckle pattern is frequently modelled as the convolution of the Airy disc and a set of δ functions.

Assuming this model, we write $T(\boldsymbol{w})$ as

$$T(\boldsymbol{w}) = \sum_{m=1}^{M} c_m \delta(\boldsymbol{w} - \boldsymbol{w}_m), \tag{9}$$

where $c_m = |c_m| \exp(\mathrm{i}\xi_m)$ is a complex constant, $\boldsymbol{w}_m$ indicates the mth speckle position, and M is the number of speckles. Unlike in the speckle interferometry case, the assumption of $s(\boldsymbol{r}) = 1$ is not valid because it carries information on scintillation. Accordingly, $\Psi_p(\boldsymbol{w})$ is interpreted as the convolution of a modulated Airy disc, $S(\boldsymbol{w})$*$P(\boldsymbol{w})$, and δ functions, $T(\boldsymbol{w})$. We assume that the extent of $S(\boldsymbol{w})$*$P(\boldsymbol{w})$ is localized around

each speckle and that such a modulated speckle carries enough information on scintillation. This will be valid if the magnitude of scintillation is not too large.

Let us consider a measurement point $(\boldsymbol{w}_a + \boldsymbol{w}_l)$ lying within an isoplanatic region of $\boldsymbol{w}_b = (0,0)$. In such a region, the wavefront phases are unchanged except for tilt, and the amplitudes are shifted by $h(\boldsymbol{w}_a + \boldsymbol{w}_l)/f$. Equations (7) and (8) then become

$$\psi_p(\boldsymbol{r}; \boldsymbol{w}_a + \boldsymbol{w}_l) = s\left(\boldsymbol{r} - \frac{h}{f}(\boldsymbol{w}_a + \boldsymbol{w}_l)\right) t(\boldsymbol{r}) \exp\left[\mathrm{i}\frac{k}{f}\boldsymbol{r}(\boldsymbol{w}_a + \boldsymbol{w}_l)\right] p(\boldsymbol{r}) \tag{10}$$

and

$$\Psi_p(\boldsymbol{w}; \boldsymbol{w}_a + \boldsymbol{w}_l) = \left\{S(\boldsymbol{w}) \exp\left[-\mathrm{i}\frac{k}{f}\boldsymbol{w} \cdot \frac{h}{f}(\boldsymbol{w}_a + \boldsymbol{w}_l)\right]\right\} * T(\boldsymbol{w} - \boldsymbol{w}_a - \boldsymbol{w}_l) * P(\boldsymbol{w}), \tag{11}$$

respectively. A light beam passing through one FS is observed separately from one passing through the other FS. Thus we define a new coordinate $\boldsymbol{w}_l$ such that its origin is coincident with $\boldsymbol{w}_a$. The wavefront through the FS is then represented as

$$\Psi_Q(\boldsymbol{w}; \boldsymbol{w}_a + \boldsymbol{w}_l) = \left\{\left\{S(\boldsymbol{w}) \exp\left[-\mathrm{i}\frac{k}{f}\boldsymbol{w} \cdot \frac{h}{f}(\boldsymbol{w}_a + \boldsymbol{w}_l)\right]\right\} * T(\boldsymbol{w} - \boldsymbol{w}_l) * P(\boldsymbol{w})\right\} Q(\boldsymbol{w}). \tag{12}$$

The function $Q(\boldsymbol{w})$ is unity inside the small aperture and zero elsewhere. Because the extent of $S(\boldsymbol{w})$*$P(\boldsymbol{w})$ is smaller than that of $T(\boldsymbol{w})$, as described above, we rewrite equation (12) as

$$\Psi_Q(\boldsymbol{w}; \boldsymbol{w}_a + \boldsymbol{w}_l) = \left\{S(\boldsymbol{w}) \exp\left[-\mathrm{i}\frac{k}{f}\boldsymbol{w} \cdot \frac{h}{f}(\boldsymbol{w}_a + \boldsymbol{w}_l)\right]\right\} * [T(\boldsymbol{w} - \boldsymbol{w}_l) Q(\boldsymbol{w})] * P(\boldsymbol{w}). \tag{13}$$

Selected δ functions $T(\boldsymbol{w})Q(\boldsymbol{w})$ are convolved with $S(\boldsymbol{w})$*$P(\boldsymbol{w})$ in this equation, while $T(\boldsymbol{w})$ is convolved with $S(\boldsymbol{w})$*$P(\boldsymbol{w})$ and then windowed with $Q(\boldsymbol{w})$ in equation (12). This indicates that $\Psi_Q(\boldsymbol{w})$ in equation (13) has errors around the edges of $Q(\boldsymbol{w})$. However, such errors will not be too serious if the speckle distribution in $T(\boldsymbol{w})$ is sparse (see next paragraph). In equation (13), $P(\boldsymbol{w})$ is shown to be unaffected by $Q(w)$. As the consequence, $p(r)$ will appear in the following equations, as if it were unaffected by $Q(w)$. If this was valid, the observed pupil images would show a perfect aperture shape. However, $P(\boldsymbol{w})$ is naturally affected by the errors around the $Q(\boldsymbol{w})$-edges. Thus the image of $p(\boldsymbol{r})$ will actually be blurred on its edges (see Fig. 4).

We here assume that the speckle distribution in $T(\boldsymbol{w})$ is sparse and that the number of speckles falling inside $Q(\boldsymbol{w})$ from the point $(\boldsymbol{w}_a+\boldsymbol{w}_l)$ is one or zero. That is to say,

$$T(\boldsymbol{w} - \boldsymbol{w}_l) Q(\boldsymbol{w}) = \begin{cases} c_m \delta(\boldsymbol{w} - \boldsymbol{w}_l - \boldsymbol{w}_m) : \boldsymbol{w}_l + \boldsymbol{w}_m \equiv \boldsymbol{w}' \subset Area[Q] \\ 0 \quad : \quad \text{elsewhere} \end{cases}, \tag{14}$$

where *Area*[*func*] denotes the non-zero area of a function *func*( ). Substituting the above equation into equation (13) and Fourier-transforming it leads to the complex amplitude distribution on the detector plane:

$$\psi_Q(\boldsymbol{r}; \boldsymbol{w}_a + \boldsymbol{w}_l) = s\left(\boldsymbol{r} - \frac{h}{f}(\boldsymbol{w}_a + \boldsymbol{w}_l)\right) c_m \exp\left(\mathrm{i}\frac{k}{f}\boldsymbol{r}\boldsymbol{w}'\right) p(\boldsymbol{r}). \tag{15}$$

Its intensity is

$$I_Q(\boldsymbol{r}; \boldsymbol{w}_a + \boldsymbol{w}_l) = s^2\left(\boldsymbol{r} - \frac{h}{f}(\boldsymbol{w}_a + \boldsymbol{w}_l)\right) |c_m|^2 p(\boldsymbol{r}). \tag{16}$$

This indicates that the intensity distribution from the point $(\boldsymbol{w}_a + \boldsymbol{w}_l)$ is shifted by $(\boldsymbol{w}_a + \boldsymbol{w}_l)h/f$, weighted by $|c_m|^2$, and observed inside the pupil.

The intensity distribution observed on the detector is obtained by integrating all the contributions passing the FS from everywhere on the solar surface:

$$I(\boldsymbol{r}; \boldsymbol{w}_a) = \int_{Area[T*Q]} \mathrm{d}\boldsymbol{w}_l \; I_Q(\boldsymbol{r}; \boldsymbol{w}_a + \boldsymbol{w}_l). \tag{17}$$

Using once more the assumption of a sparse speckle distribution, this becomes

$$I(\boldsymbol{r}; \boldsymbol{w}_a) = \sum_{m=1}^{M} \int_{Area[Q]} \mathrm{d}\boldsymbol{w}' \; I_Q\left(\boldsymbol{r}; \boldsymbol{w}_a + \boldsymbol{w}' - \boldsymbol{w}_m\right), \tag{18}$$

and finally leads to, as in Appendix A,

$$I(\boldsymbol{r}; \boldsymbol{w}_a) = \left[\left|\psi_0\left(\boldsymbol{r} - \frac{h}{f}\boldsymbol{w}_a\right)\right|^2 * \left|T\left(-\frac{f}{h}\boldsymbol{r}\right)\right|^2 * Q\left(\frac{f}{h}\boldsymbol{r}\right)\right] p(\boldsymbol{r}). \tag{19}$$

At the point $\boldsymbol{w}_b = (0,0)$,

$$I(\boldsymbol{r}; \boldsymbol{w}_b) = \left[|\psi_0(\boldsymbol{r})|^2 * \left|T\left(-\frac{f}{h}\boldsymbol{r}\right)\right|^2 * Q\left(\frac{f}{h}\boldsymbol{r}\right)\right] p(\boldsymbol{r}). \tag{20}$$

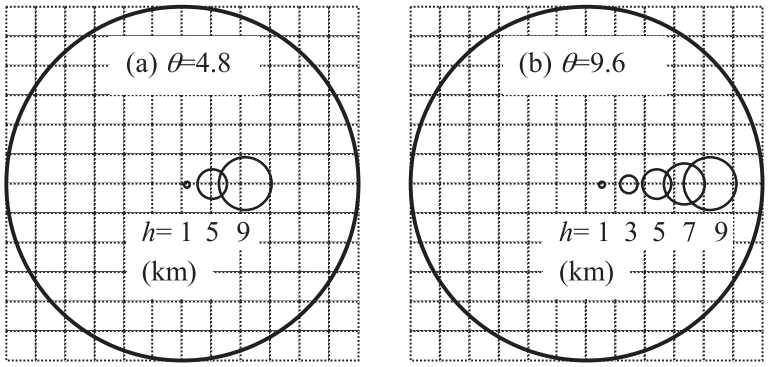

Figure 2. Correlation–point spread function sizes for various heights of turbulent layers when θ = (a) 4.8 and (b) 9.6 arcsec.

The observed scintillation is blurred by both the δ function pattern and the FS shape. The degree of blur is dependent on the height of the turbulent layer causing the scintillation.

2.3 Solar SCIDAR technique

In our solar SCIDAR, unlike in the night-time case, $|\psi_0(\boldsymbol{r})|^2$ itself is not observed, as shown in equations (19) and (20). We therefore calculate $\langle I(\boldsymbol{r})\rangle$ instead of $\langle|\psi_0(\boldsymbol{r})|^2\rangle$ and assume

$$\langle I\,(r)\rangle = \left\langle|\psi_0\,(r)|^2\right\rangle = \text{const.} \tag{21}$$

The normalized intensity fluctuations are then

$$I_a\,(\boldsymbol{r}) = \frac{I\,(\boldsymbol{r};\boldsymbol{w}_a) - \langle I\,(\boldsymbol{r};\boldsymbol{w}_a)\rangle}{\langle I\,(\boldsymbol{r};\boldsymbol{w}_a)\rangle} = \left[F\left(\boldsymbol{r} - \frac{h}{f}\boldsymbol{w}_a\right) * \left|T\left(-\frac{f}{h}\boldsymbol{r}\right)\right|^2 * Q\left(\frac{f}{h}\boldsymbol{r}\right)\right] p\,(\boldsymbol{r})\,. \tag{22}$$

Similarly,

$$I_b\,(\boldsymbol{r}) = \frac{I\,(\boldsymbol{r};\boldsymbol{w}_b) - \langle I\,(\boldsymbol{r};\boldsymbol{w}_b)\rangle}{\langle I\,(\boldsymbol{r};\boldsymbol{w}_b)\rangle} = \left[F\,(\boldsymbol{r}) * \left|T\left(-\frac{f}{h}\boldsymbol{r}\right)\right|^2 * Q\left(\frac{f}{h}\boldsymbol{r}\right)\right] p\,(\boldsymbol{r})\,. \tag{23}$$

The cross-correlation of $I_a(\boldsymbol{r})$ and $I_b(\boldsymbol{r})$ is executed and normalized only within an overlapped region of $p(\boldsymbol{r})$. Consequently, the influence of $p(\boldsymbol{r})$ disappears from the following equation:

$$I_a\,(\boldsymbol{r}) \otimes I_b\,(\boldsymbol{r}) = \left[F\left(\boldsymbol{r} - \frac{h}{f}\boldsymbol{w}_a\right) \otimes F\,(\boldsymbol{r})\right] * \left[\left|T\left(\frac{f}{h}\boldsymbol{r}\right)\right|^2 \otimes \left|T\left(\frac{f}{h}\boldsymbol{r}\right)\right|^2\right] * \left[Q\left(\frac{f}{h}\boldsymbol{r}\right) \otimes Q\left(\frac{f}{h}\boldsymbol{r}\right)\right], \tag{24}$$

where $\otimes$ denotes a correlation operation. As in the night-time SCIDAR, we assume that the first term yields a correlation peak and zero-mean contaminations. The ensemble average of the cross-correlation for the multiple-layer case becomes, as a consequence,

$$\langle I_a\,(\boldsymbol{r}) \otimes I_b\,(\boldsymbol{r})\rangle = \int_0^\infty \mathrm{d}h\; B_h\left(x - \frac{h}{f}u_a, y, h\right) * \left\langle\left|T\left(\frac{f}{h}\boldsymbol{r}\right)\right|^2 \otimes \left|T\left(\frac{f}{h}\boldsymbol{r}\right)\right|^2\right\rangle * \left[Q\left(\frac{f}{h}\boldsymbol{r}\right) \otimes Q\left(\frac{f}{h}\boldsymbol{r}\right)\right]. \tag{25}$$

This is the formula for our solar SCIDAR, in contrast to equation (5) for the night-time SCIDAR.

From equation (25), we note the following points.

(i) One, not three, correlation peak appears at the position θh. This is because our SCIDAR technique takes the cross-correlation of two scintillation patterns observed separately, while the night-time SCIDAR uses the autocorrelation of a scintillation pattern containing dual shadow distributions.

(ii) The last two terms act as a point spread function (PSF), degrading correlation peaks. We hereafter refer to it as a correlation-PSF. The size of the correlation-PSF depends on h (see Fig. 2).

(iii) Because the correlation-PSF does not alter the positions of peaks, we can derive information on turbulent-layer heights from them.

(iv) The second term $\langle|T|^2 \otimes |T|^2\rangle$ has the same statistics as the Fourier transform of the so-called speckle transfer function (Labeyrie 1970; Dainty 1975; Roddier 1974). It contains a weak core and a strong halo whose size is comparable to the seeing disc. Thus, severe seeing broadens correlation peaks, in particular ones originating from higher layers, and makes the method lose sensitivity to higher-layer turbulence. If the core was dominant, our solar SCIDAR could provide information nearly equivalent to that of the night-time SCIDAR.

(v) The third term is the autocorrelation of the FS used. To narrow the correlation-PSF, the size of FSs should be as small as possible. However, the FS must be large enough to pass a speckle modulated by scintillation. Therefore, there is always an effect from finite-sized FSs in our SCIDAR technique.

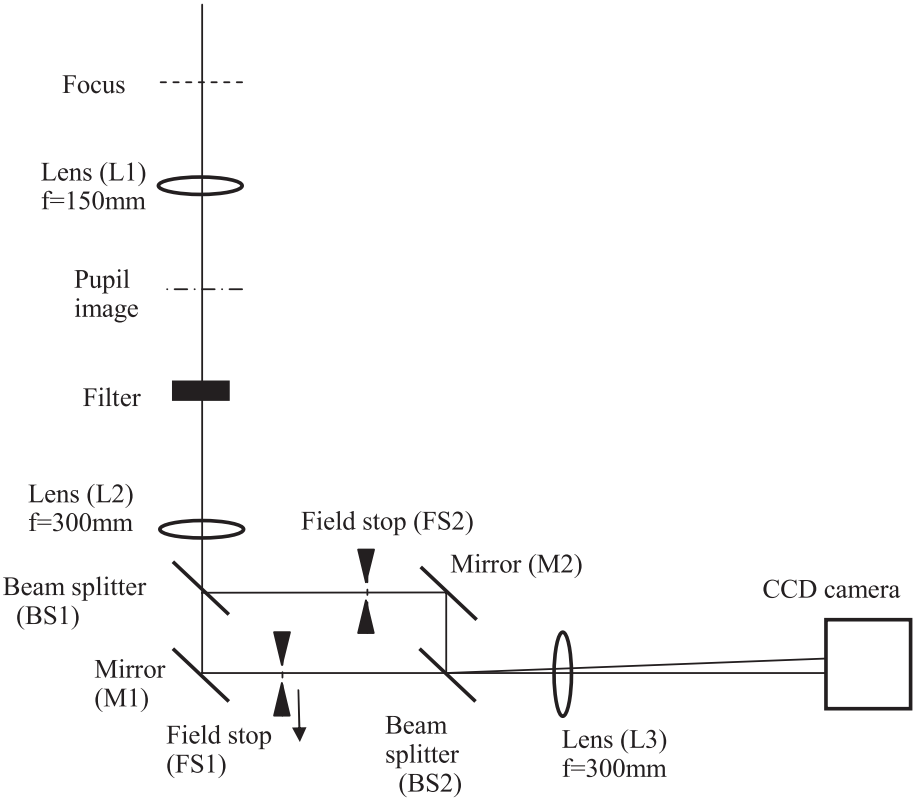

Figure 3. Optical setup for solar SCIDAR observations.

Fig. 2 illustrates the effect of the correlation-PSF. The rings correspond to the correlation-PSF sizes for various heights of the turbulent layer for (a) $\theta = 4.8$ and (b) 9.6 arcsec, when the sizes of FSs and the seeing disc are 0.5 and 1.5 arcsec, respectively. As can be seen, the extent of the correlation peaks increases with height. When θ is small, peaks of various heights tend to overlap each other, and the interpretation of peak structure is difficult. On the other hand, too large a value of θ lowers the upper limit of height to be probed.

In the speckle interferometry, the term $\langle |T|^2 \otimes |T|^2 \rangle$ is ordinarily estimated from short-exposure images of a point-like reference star, whose statistics are regarded to be same as those of the target. Such a point-like object is, unfortunately, unavailable in solar observations. Thus, we need to develop a method of estimating this term in order to derive $C_n^2(h)$ from the ensemble-averaged cross-correlation.

The present solar SCIDAR technique is not generalized, and thus has no sensitivity to ground-level turbulence. That is to say, in equation (25) no peak will appear at the centre of the correlation plane because $B_h(x, y, h)$ becomes zero when $h = 0$. Central peaks can, however, be seen with positive or negative values in the correlation images shown in Section 4. These peaks result from the knife-edge effect induced by FSs on the image plane. We should note that equation (25) does not involve such a knife-edge effect because the derivation of the equation was made under geometric considerations.

The above-mentioned points (iv) and (v) account for the problems of (A) image degradation and (B) finite-sized aperture described in Section 1, respectively. The problem of (C) knife edge will be discussed in Section 5.1.

3 OBSERVATION AND SETUP

Fig. 3 shows the optical setup of our SCIDAR system. The lens L1 collimates the light beam to form a pupil image, and then the lenses L2 and L3 relay it onto the detector. The light beam is split into two paths (M1–FS1 and FS2–M2), and then returns to the same path at the beam splitter BS2. A small tilt is added to BS2 to form the two pupil images at different positions on the detector. Solar images on the FS-planes are sampled by FSs. An FS (FS1) is put on a movable stage with a micrometer and can be shifted by an arbitrary amount. The CCD camera used was the Hamamatsu Photonics C4880-80, specified with 656 × 494 pixels, a 9.9-μm pixel size, a readout frequency of 28 Hz, and a 12-bit dynamic range. The diameter of pupil images on the camera was 2.80 mm, which corresponds to 282 pixels.

When a lens is added to the camera, two solar images sampled by the FSs can be simultaneously observed. This setup was used to check the size and shape of the FSs and the relative shift between the fields of view through two FSs. We fixed the sizes of FSs to be 0.5-arcsec square.

Observations were conducted using the 60-cm domeless solar telescope of Hida Observatory, Japan, from 2012 May 27 to June 1. During this period, the weather unfortunately tended to be cloudy. We monitored clouds and tried to avoid them when starting acquisition. We changed θ from 1.6 to 9.6 arcsec with an interval of 1.6 arcsec and acquired 500 frames per set. The observational wavelength and bandwidth were 450 and 80 nm, respectively. When acquiring images, we usually operated an AO system, which was put upstream of the SCIDAR

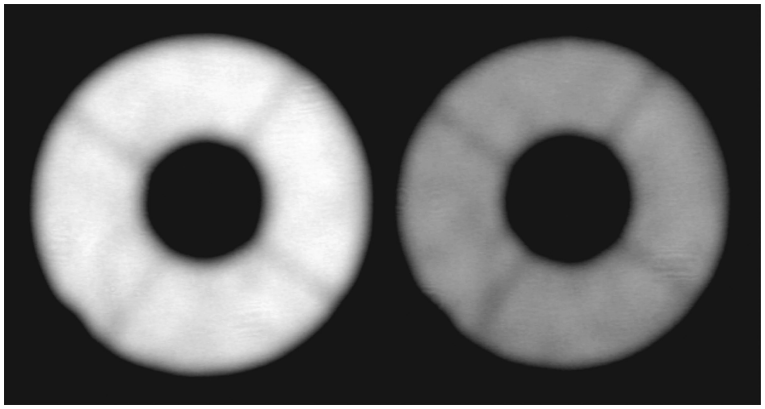

Figure 4. One of the observed images. The images of the 60-cm pupil have diameters of 282 pixels.

system. As a sensing target for AO, we used a small sunspot that was about 10 arcsec from a SCIDAR target, because seeing conditions were such that AO did not work well using granules as a target.

Fig. 4 shows one of the frames observed with $\theta = 3.2$ at 08:37:47 on May 27. As previously noted, the edges and spiders are blurred by the influence of small FSs. The difference in brightness of the two pupil images was caused by the inequality of reflection and transmission of the beam splitters. However, this does not affect the results, because of the normalization of intensity fluctuation as in equations (22) and (23).

The observed data were usually processed as follows: a window was defined so as to distinguish regions unaffected by the aperture edges and the spiders from those that were affected. The subsequent flat-fielding and cross-correlating in equation (25) were performed only within the window. The data for flat-fielding were derived by temporally averaging the observed data set. Each frame was then divided by the flat-fielding data so that fixed noisy patterns were removed. The ensemble average of the flat-fielded frames became constant as a result. In this manner, the assumption of equation (21) becomes valid and the derivation of normalized intensity fluctuations as in equations (22) and (23) are fair. Fig. 5 shows the first three images of intensity fluctuations, excluding spider and edge regions, where the top images correspond to the image in Fig. 4. Comparing left and right images, we can see partially similar shadows with small shifts.

4 RESULTS

Tables 1 –3 summarize the observational results on May 27, May 31 and June 1, respectively. They only contain cases in which peaks originating from scintillation shadows (SCI-peaks) were detected. Columns 7 and 8 list the distances and heights from the telescope to turbulent layers. It should be noted that these numbers show just the calculated results and do not reflect the accuracy of the method. All the values of height in the tables refer to height above the observatory. The height above sea level is obtained by adding the altitude of the Hida Observatory, 1276 m. In column 9, 'High' or 'Low' indicates that SCI-peaks appear with a high or low contrast on the correlation planes. When we saw two SCI-peaks on the correlation plane, we wrote '2nd' in the column. The central peaks caused by the knife-edge effect (KE-peaks) reveal a variety of shapes, as positive (P), negative (N) or a mixture of both (Mix).

Fig. 6 shows examples of correlation images and their profiles. The sizes of circles in the correlation images are twice those in Fig. 5. The correlation images (a)–(d) exhibit not only SCI-peaks along the $+x$-direction, but also KE-peaks of various types at the centre. The curves in the graphs (e)–(h) show profiles of correlation images along the $+x$ (solid curve) and $+y$ (dashed curve) directions. Obviously, the SCI-peaks are shifted in proportion to θ and their values tend to be lower for larger θ. In profiles (f) and (h) with the same θ, but with a time interval of 82 min, SCI-peaks appear at similar positions with similar peak strengths. From these results, we think that the deterioration of the peak values results from the anisoplanatism between two regions sampled by the FSs. Therefore, the separation of the FSs should be as small as possible in our solar SCIDAR, from the point of isoplanatism. The vertical plots in (e)–(h) show non-zero bumpy profiles, while ideally they should be zero and flat. We note that more frames are necessary to increase the signal-to-noise ratio of the correlation images.

From the tables, 51 results among 125 measurements are excluded because any SCI-peaks were not clearly detected. There were three cases of failure, as follows.

Case 1 (35 results): Shadows caused by clouds floating in lower layers were dominant. In this case, a strong broad correlation peak ordinarily appears at the centre of the correlation plane. Fig. 7(a) is a correlation image in the case for $\theta = 3.2$ and an observational time of 11:46:42 on May 27. After 2.5 min, the correlation image was as shown in Fig. 7(b) ($\theta = 4.8$, M27-30). In addition to the pattern in (a), there is a SCI-peak. We consider that the effect of clouds decreased within 2.5 min. Results like those in Fig. 7(b) appear with the comment 'Cloud' in the list.

Case 2 (12 results): SCI-peaks overlapped a KE-peak at the centre. This occurred when θ and/or h were small. Most of the results with $\theta = 1.6$ fell into this category. Only one result (J1-7) listed in the tables is shown in Fig. 8(a). We judged that the central KE-peak was weak and thus SCI-peaks were detectable. In Fig. 8(b), for comparison, it is hard to discriminate a SCI-peak from a KE-peak.

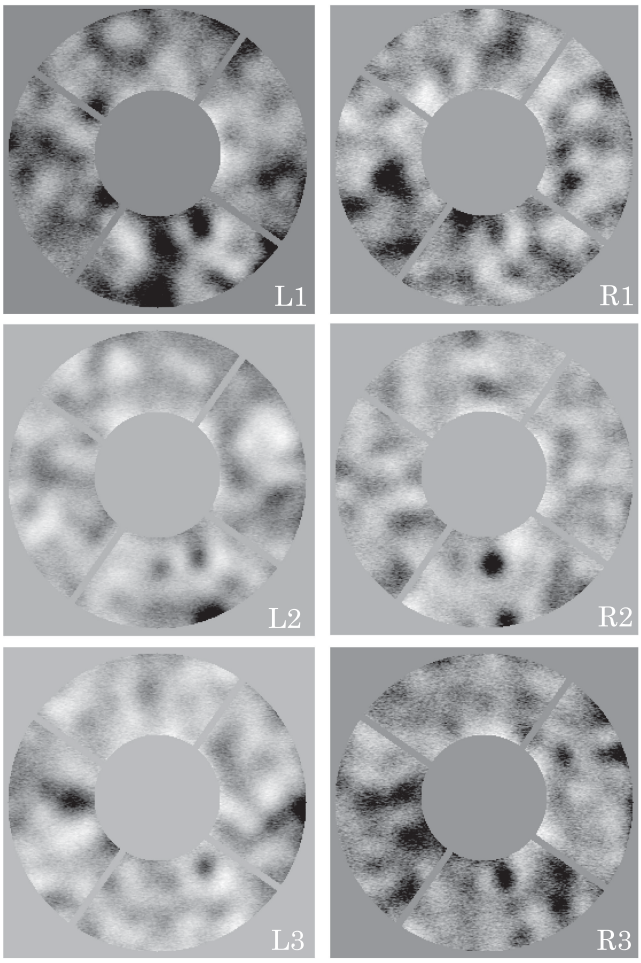

Figure 5. First three left (left column) and right (right column) pupil images, processed by flat-fielding and masking. Image acquisition was performed at 28 Hz. The top two images are as in Fig. 4. The diameters of outer-circle edges are 238 pixels and correspond to 50.6 cm on the pupil.

Case 3 (4 results): SCI-peaks were indistinguishable from background, including noise peaks. This does not indicate that there was no turbulent layer, but only, say, that our SCIDAR technique could not detect it. We will discuss the detectable range of our method later.

There were two results for which multiple layers were detected. The first one is shown in Fig. 8(a): a compact strong peak and a broad weaker overlap, the peaks being caused by lower- and higher-layer turbulence, respectively. The other one (J1-14) is shown in Fig. 9(a). We recognize a compact weak peak and a broad peak indicated by the arrows. Fig. 9(b) is the result 2.5 min before (a), which was excluded from the table because of cloud effects. Although similar patterns caused by clouds appear at the centre in both (a) and (b), the cloud effects in (a) are weaker.

Most of the distances detected in the observations were within 2500–3500 m, as shown in the tables. There are two reasons why peaks at shorter distances were not detected. The first is that scintillation itself becomes weaker in a short distance. The other is because a peak appears near the centre of the correlation plane and then tends to overlap a KE-peak. At greater distances, scintillation patterns originating from a distant turbulent layer are severely blurred, as described in equations (19) and (20), and then are not detectable. From these considerations, we believe that there is a distance range within which turbulent layers can be detected by our solar SCIDAR method.

We had expected that the use of AO would relax the influence of seeing so that $\langle |T|^2 \otimes |T|^2 \rangle$ could have a stronger core and a small weak halo. Thus we used an AO system in the SCIDAR observations. Column 4 in Tables 1–3 shows the AO situation at each SCIDAR observation as operating wavefront compensation (AO), tip-tilt correction (TT) or both (AO+TT). Our experience showed that our current AO system was capable of attaining a Strehl ratio of less than 0.1 under 1.5-arcsec seeing (Miura et al. 2012). However, through our SCIDAR observations, differences were negligible between results with and without AO correction in comparisons of detection ratio and peak contrast.

5 DISCUSSIONS

5.1 Knife-edge effect

Fig. 10 illustrates the generation of knife-edge shadows by the edges of FSs. Two points A and B on the solar surface are imaged at the two vertical edges of a FS, respectively. Image A, being blurred by atmospheric turbulence, is partially cut by the edge. Shadows of pupil-plane

Table 1. Observational results on 2012 May 27.

No.	Time (JST)	Exposure time (ms)	AO	Zenith angle (°)	θ (arcsec)	Distance (m)	Height (m)	SCI peak	KE peak	Comments
M27-1	8:34:45	8.6	AO	44.4	3.2	3537	2527	–	N	–
M27-2	8:37:57	8.6	AO+TT	43.8	3.2	3537	2553	High	N	–
M27-3	8:39:05	8.6	AO+TT	43.5	4.8	3265	2368	High	–	–
M27-4	8:42:03	8.6	AO+TT	43	4.8	3355	2454	–	P	–
M27-5	8:43:21	8.6	AO+TT	42.7	6.4	3197	2349	–	N	–
M27-6	8:44:30	8.6	AO+TT	42.4	6.4	3129	2310	–	P	–
M27-7	8:48:10	8.6	AO+TT	41.7	8.0	3101	2316	–	N	–
M27-8	8:49:26	8.6	AO+TT	41.4	8.0	2993	2245	–	N	–
M27-9	8:51:23	8.6	AO+TT	41.1	9.6	2993	2255	–	N	–
M27-10	8:52:58	8.6	AO+TT	40.7	9.6	3151	2389	–	P	–
M27-11	9:57:48	5.7	TT	28.2	3.2	3129	2757	– High	P	–
M27-12	10:00:11	5.7	TT	27.8	4.8	3355	2968	–	P	–
M27-13	10:01:22	5.7	TT	27.6	4.8	3401	3014	–	Mix	–
M27-14	10:02:43	5.7	TT	27.3	6.4	3333	2962	–	–	–
M27-15	10:04:26	5.7	TT	27	6.4	3299	2939	–	P	–
M27-16	10:05:40	5.7	TT	26.8	8.0	3210	2865	–	–	–
M27-17	10:06:47	5.7	TT	26.6	8.0	3238	2895	–	–	–
M27-18	10:07:58	5.7	TT	26.4	9.6	3197	2863	–	–	–
M27-19	10:09:06	5.7	TT	26.2	9.6	3151	2828	–	P	–
M27-20	10:53:28	5.7	TT	19	3.2	3129	2958	–	N	–
M27-21	10:54:39	5.7	TT	18.8	3.2	3129	2962	–	N	–
M27-22	10:55:54	5.7	TT	18.7	4.8	2857	2706	–	Mix	–
M27-23	10:57:09	5.7	TT	18.5	4.8	2857	2709	–	P	–
M27-24	10:58:23	5.7	TT	18.4	6.4	2959	2807	–	P	–
M27-25	11:00:37	5.7	TT	18.1	6.4	2925	2780	–	P	–
M27-26	11:02:19	5.7	TT	17.9	8.0	2993	2848	–	N	–
M27-27	11:03:20	5.7	TT	17.7	8.0	2993	2851	–	N	–
M27-28	11:47:53	7.1	TT	14.8	4.8	2857	2762	–	P	Cloud
M27-29	11:49:09	7.1	TT	14.8	4.8	2857	2762	–	P	Cloud
M27-30	11:50:24	7.1	TT	14.8	6.4	2789	2696	–	P	Cloud
M27-31	11:52:26	7.1	TT	14.8	6.4	2891	2795	–	P	Cloud
M27-32	11:53:39	7.1	TT	14.8	8.0	3020	2920	–	–	Cloud
M27-33	11:54:52	7.1	TT	14.9	8.0	3020	2918	–	Mix	Cloud
M27-34	11:56:06	7.1	TT	14.9	9.6	2947	2848	–	Mix	Cloud

Note. AO: use of an adaptive optics system; θ: angular distance between measurement points; (m): distance and height from the observatory to a turbulent layer; SCI: scintillation peak; KE: knife-edge peak.

phases then appear on the pupil-conjugate plane. On the other image, occultation by the knife edge is complementary, and the shadow pattern B becomes negative as a result. The shadow pattern observed with the detector is the sum of patterns A and B weighted by their brightness.

In our observations, we used FSs of 0.5-arcsec square. The FS has two vertical and two horizontal knife edges, all of which are regarded as being within an isoplanatic region. There is a special case that intensity distributions along the two vertical edges are identical, as for position (a) in Fig. 11. In this case, the two shadow patterns caused by the two edges are complementary and total shadows tend to vanish as a consequence. No KE-peak then appears on the correlation plane. However, such a case is infrequent because the solar surface is filled with asymmetric fine structures.

In our technique, the two FSs usually sample solar structures at different positions. Thus, the positional relationship between edges and solar structures changes on each FS. When the right FS is at the position (b) in Fig. 11, the left and right vertical edges are on dark and bright solar structures, respectively, and shadows caused by the right edge become dominant. Because this positional relation is the same as on the left FS, the same shadow pattern appears on both pupil images. This is the case when a KE-peak is positive at the centre on the correlation plane. The other position (c) is the case of yielding a negative KE-peak. The dominant edge causing shadows differs on the two FSs.

There are cases where vertical and horizontal edges make different types of KE-peaks, positive or negative. The KE-peaks on the correlation plane then become a mixture of the two peaks, as shown in Fig. 6(d).

5.2 Assumption of uniform intensity distribution

To derive the solar SCIDAR formula, we assumed a uniform intensity distribution on the solar surface. Of course, this is not strictly true. Let us consider here the case when that assumption is removed.

Table 2. Observational results on 2012 May 31.

No.	Time (JST)	Exposure time (ms)	AO	Zenith angle (°)	θ (arcsec)	Distance (m)	Height (m)	SCI peak	KE peak	Comments
M31-1	11:04:51	5.7	AO+TT	17.1	3.2	2585	2470	High	P	–
M31-2	11:05:50	5.7	AO+TT	17	4.8	2539	2428	High	P	–
M31-3	11:06:58	5.7	AO+TT	16.8	4.8	2811	2691	–	Mix	–
M31-4	11:08:34	5.7	AO+TT	16.7	6.4	2891	2769	–	N	–
M31-5	11:09:39	5.7	AO+TT	16.5	6.4	2789	2674	–	N	–
M31-6	11:10:39	5.7	AO+TT	16.4	8.0	2666	2558	–	Mix	–
M31-7	11:11:45	5.7	AO+TT	16.3	8.0	2748	2637	–	Mix	–
M31-8	11:13:59	5.7	AO+TT	16.1	9.6	2607	2505	Low	P	–
M31-9	14:45:36	7.1	AO+TT	40.7	4.8	2902	2200	Low	Mix	–
M31-10	14:46:43	7.1	AO+TT	41	4.8	2267	1711	Low	P	Cloud
M31-11	14:48:02	5.7	AO+TT	41	6.4	2823	2130	–	–	–
M31-12	14:49:01	5.7	AO+TT	41.2	6.4	2483	1868	–	–	Cloud
M31-13	14:50:21	5.7	AO+TT	41.7	8.0	2775	2072	Low	N	–
M31-14	14:54:37	5.7	AO+TT	42.5	9.6	2766	2039	Low	–	–
M31-15	15:34:20	7.1	AO+TT	50.8	8.0	2829	1788	Low	Mix	–
M31-16	15:35:33	7.1	AO+TT	51	8.0	2829	1781	Low	Mix	–
M31-17	15:37:46	7.1	AO+TT	51.2	9.6	2698	1691	Low	Mix	–
M31-18	16:08:34	7.1	AO+TT	57.4	4.8	2902	1563	Low	P	Cloud
M31-19	16:09:43	7.1	AO+TT	57.7	4.8	2811	1502	Low	P	Cloud
M31-20	16:10:52	7.1	AO+TT	57.9	6.4	3095	1645	Low	N	–
M31-21	16:12:00	7.1	AO+TT	58.1	6.4	2993	1581	Low	N	–
M31-22	16:14:53	7.1	AO+TT	58.7	8.0	2503	1300	Low	P	–
M31-23	16:16:05	7.1	AO+TT	59	8.0	2666	1373	Low	P	–
M31-24	16:18:35	7.1	AO+TT	59.4	9.6	2698	1373	Low	N	–

Note. AO: use of an adaptive optics system; θ: angular distance between measurement points; (m): distance and height from the observatory to a turbulent layer; SCI: scintillation peak; KE: knife-edge peak.

Table 3. Observational results on 2012 June 1.

No.	Time (JST)	Exposure time (ms)	AO	Zenith angle (°)	θ (arcsec)	Distance (m)	Height (m)	SCI peak	KE peak	Comments
J1-1	7:27:33	14.0	AO+TT	57.7	3.2	2857	1526	Low	Mix	–
J1-2	7:28:43	14.0	AO+TT	57.5	4.8	2675	1437	–	P	–
J1-3	7:29:50	14.0	AO+TT	57.2	4.8	2585	1400	–	P	–
J1-4	7:33:32	11.0	AO+TT	56.5	8.0	2693	1487	Low	P	–
J1-5	7:36:47	11.0	AO+TT	55.8	9.6	2811	1580	Low	Mix	–
J1-6	7:38:25	11.0	AO+TT	55.5	9.6	2698	1528	Low	Mix	–
J1-7	10:03:34	5.7	AO+TT	26.8	1.6	3673 8434	3278 7528	High 2nd	P	– –
J1-8	11:47:30	7.1	AO+TT	14	3.2	3605	3498	Low	N	Cloud
J1-9	11:50:07	7.1	AO+TT	14	6.4	2721	2640	–	P	–
J1-10	16:11:24	11.0	AO+TT	57.9	8.0	2857	1518	Low	P	–
J1-11	16:12:32	11.0	AO+TT	58.1	8.0	2993	1581	Low	Mix	–
J1-12	16:13:41	11.0	AO+TT	58.4	9.6	2879	1509	Low	N	–
J1-13	16:14:51	11.0	AO+TT	58.6	9.6	2879	1500	Low	–	–
J1-14	17:06:21	11.0	TT	68.8	4.8	2721 9023	984 3263	- 2nd	P	Cloud
J1-15	17:07:29	11.0	TT	69.1	6.4	2959	1055	–	–	–
J1-16	17:08:39	11.0	TT	69.3	8.0	2965	1048	Low	N	–
J1-17	17:09:48	11.0	TT	69.5	9.6	2902	1016	Low	N	–

Note. AO: use of an adaptive optics system; θ: angular distance between measurement points; (m): distance and height from the observatory to a turbulent layer; SCI: scintillation peak; KE: knife-edge peak.

Using $g(\boldsymbol{w})$ as the intensity distribution on the solar surface, equation (16) changes to

$$I_Q(\boldsymbol{r}; \boldsymbol{w}_a + \boldsymbol{w}_l) = s^2 \left(\boldsymbol{r} - \frac{h}{f}(\boldsymbol{w}_a + \boldsymbol{w}_l) \right) |c_m|^2 \, g(\boldsymbol{w}_a + \boldsymbol{w}_l) \, p(\boldsymbol{r}) \,. \tag{26}$$

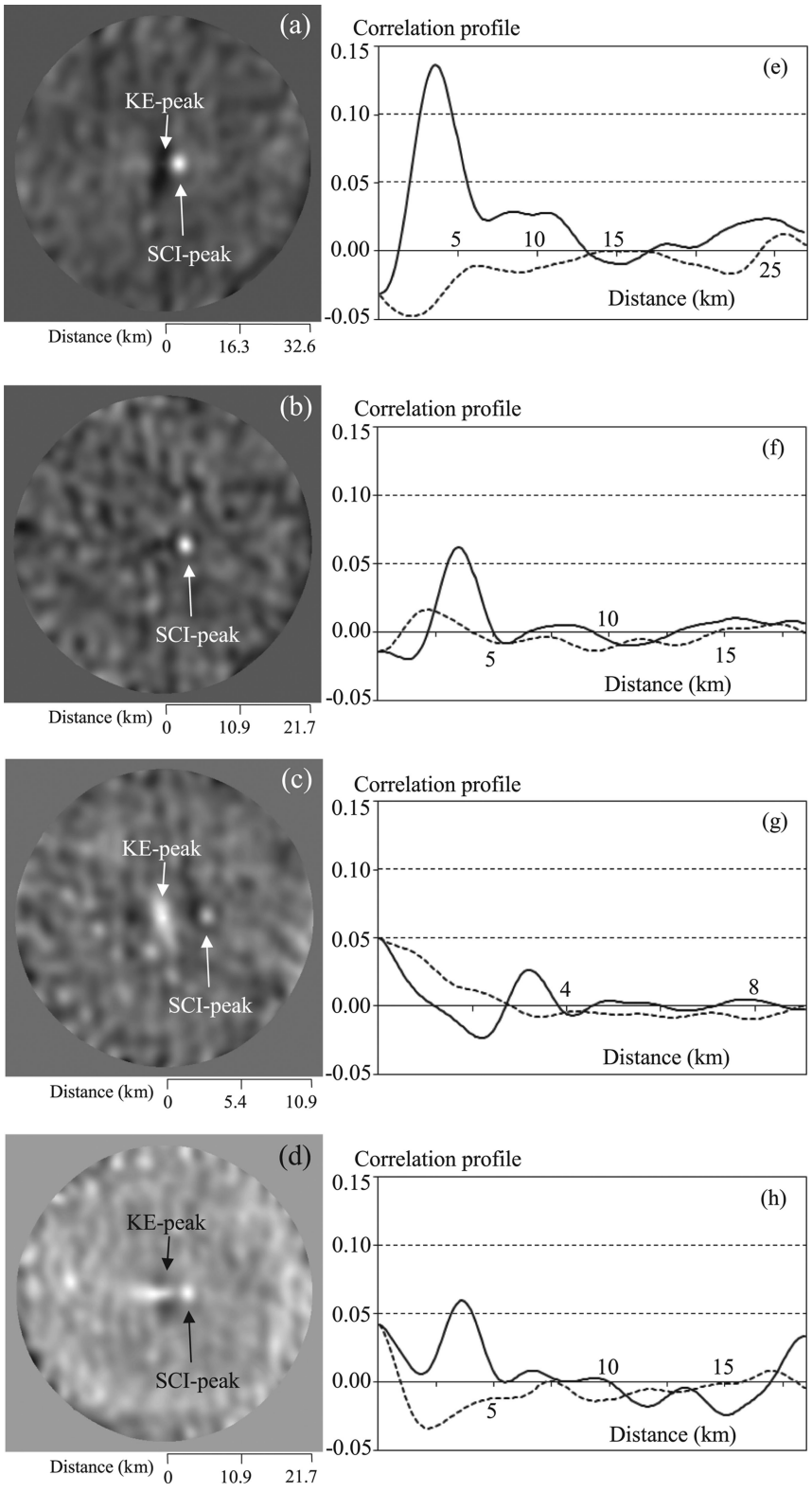

Figure 6. Correlation images with various knife-edge peaks: (a) negative ($\theta = 3.2$, M27-2), (b) none ($\theta = 4.8$, M27-3), (c) positive ($\theta = 9.6$, M27-10), and (d) mixture ($\theta = 4.8$, M27-13). Graphs (e)–(h) correspond to (a)–(d), respectively. The solid and dashed curves in graphs (e)–(h) show 200 correlation values along the $+x$ and $+y$ axes from the centre of the images (a)–(d), respectively.

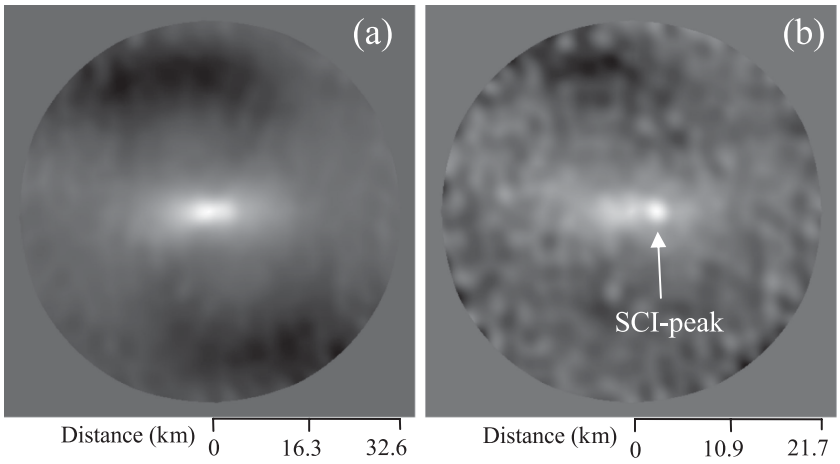

Figure 7. Correlation images affected (a) strongly and (b) weakly by clouds.

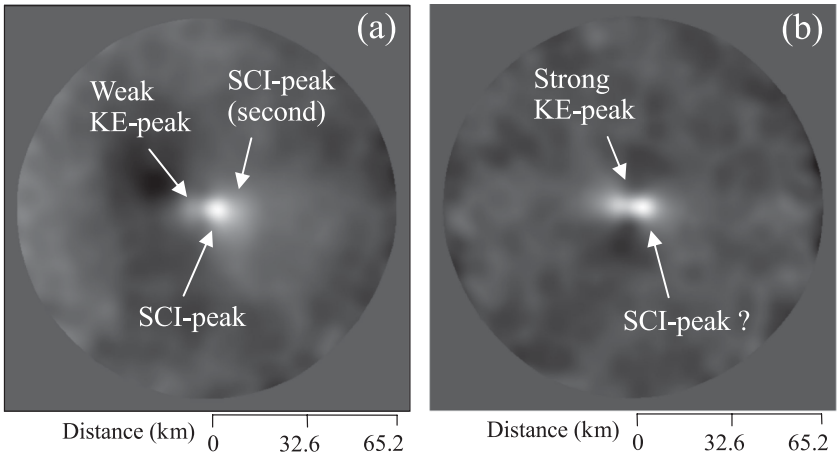

Figure 8. Correlation images with $\theta = 1.6$ arcsec. (a) SCI-peaks can be distinguished from a weak KE-peak. (b) A SCI-peak fully overlaps a KE-peak.

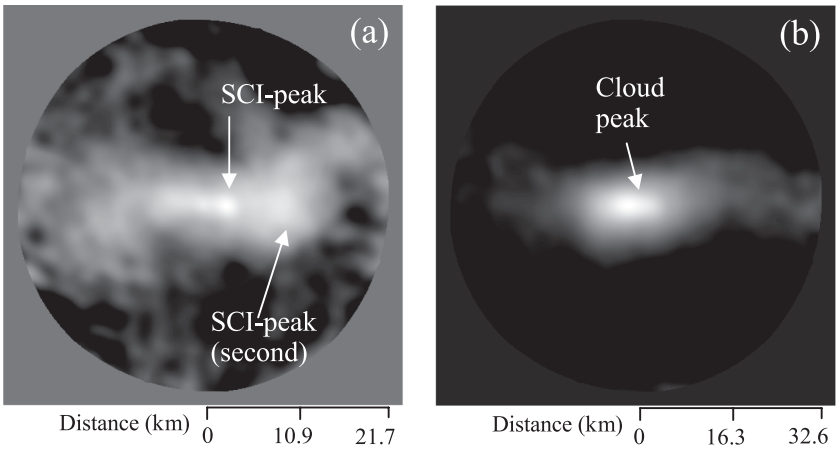

Figure 9. (a) Two SCI-peaks are confirmed, in spite of the effects of clouds. (b) Only a cloud peak appears.

For the purposes of discussion, we consider a simple object, $g(\boldsymbol{w}) = 1 + \delta(\boldsymbol{w} - \boldsymbol{w}_{\rm noise})$. The intensity distribution observed on the detector $I(\boldsymbol{r};\, \boldsymbol{w}_a)$ is obtained by substituting equation (26) into (17). The integration of the first term in $g(\boldsymbol{w})$ is given above in equation (19). The calculation of the second term is straightforward because of the integration of a δ function. Finally,

$$I\,(\boldsymbol{r};\boldsymbol{w}_a) = \left[\left|\psi_0\left(\boldsymbol{r} - \frac{h}{f}\boldsymbol{w}_a\right)\right|^2 * \left|T\left(-\frac{f}{h}\boldsymbol{r}\right)\right|^2 * Q\left(\frac{f}{h}\boldsymbol{r}\right) + \left|\psi_0\left(\boldsymbol{r} - \frac{h}{f}\boldsymbol{w}_{\rm noise}\right)\right|^2 |c_m|^2\right] p\,(\boldsymbol{r})\,. \tag{27}$$

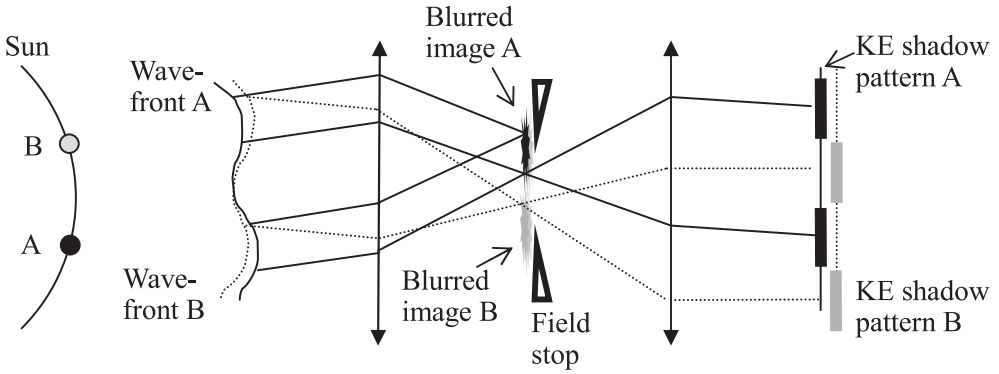

Figure 10. Generation of knife-edge shadows.

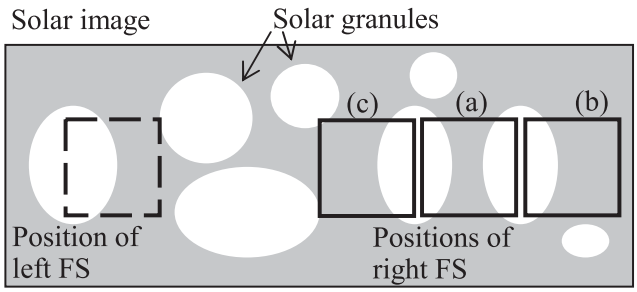

Figure 11. Positional relations between solar granules and vertical edges of field stops, accounting for yielding (a) no, (b) positive and (c) negative knife-edge peaks.

The deviations from uniform intensity yield undesirable additional shadows at different positions from the true scintillation shadows. They deform scintillation shadows and then may cause some shifts on peak positions. We therefore conclude that our solar SCIDAR should be operated on regions that are as uniform as possible. At the very least, it should not be used around sunspots.

5.3 Assumption of a sparse speckle distribution

In the formulation of our solar SCIDAR technique, the sparse speckle assumption, in which the number of speckles falling on $Q(\boldsymbol{w})$ from a point is one or zero, is important. However, this will break down under poor seeing conditions. In this section, we discuss what occurs when some speckles pass through the FSs.

To simplify the discussion, we assume that two speckles pass through the FSs. Equation (14) then changes to

$$T(\boldsymbol{w}-\boldsymbol{w}_l)\,Q(\boldsymbol{w}) = c_m\delta(\boldsymbol{w}-\boldsymbol{w}_l-\boldsymbol{w}_m) + c_n\delta(\boldsymbol{w}-\boldsymbol{w}_l-\boldsymbol{w}_n)\,. \tag{28}$$

The intensity distribution is, as a result,

$$I_Q(\boldsymbol{r};\boldsymbol{w}_a+\boldsymbol{w}_l) = s^2\left(\boldsymbol{r}-\frac{h}{f}(\boldsymbol{w}_a+\boldsymbol{w}_l)\right)\left\{|c_m|^2+|c_n|^2+2\,|c_m|\,|c_n|\cos\left[\frac{k}{f}r(\boldsymbol{w}_m-\boldsymbol{w}_n)+\xi_m-\xi_n\right]\right\}p(\boldsymbol{r})\,. \tag{29}$$

Consider a special case $c_m = c_n$. Then,

$$I_Q(\boldsymbol{r};\boldsymbol{w}_a+\boldsymbol{w}_l) = s^2\left(\boldsymbol{r}-\frac{h}{f}(\boldsymbol{w}_a+\boldsymbol{w}_l)\right)|c_m|^2\,M(\boldsymbol{r})\,p(\boldsymbol{r})\,, \tag{30}$$

where

$$M(r) = 1+\cos\left[\frac{k}{f}r(\boldsymbol{w}_m-\boldsymbol{w}_n)\right]. \tag{31}$$

Similarly, at the other measurement point $\boldsymbol{w}_b = (0,0)$,

$$I_Q(\boldsymbol{r};\boldsymbol{w}_b+\boldsymbol{w}_l) = s^2\left(\boldsymbol{r}-\frac{h}{f}\boldsymbol{w}_l\right)|c_m|^2\,M(\boldsymbol{r})\,p(\boldsymbol{r})\,. \tag{32}$$

The additional term $M(\boldsymbol{r})$ modulates the two scintillation patterns, one of which is shifted, with the same cosine function. In other words, the relative positions between the scintillation patterns and the modulation pattern differ on each pupil image. Fig. 12(a) illustrates two scintillation patterns without the modulation, with a shift of θh between them. Of course, from the correlation between them, we can derive θh. On the other hand, when the modulation is not negligible, as shown in Fig. 12(b), only part of the scintillation patterns remains. If the

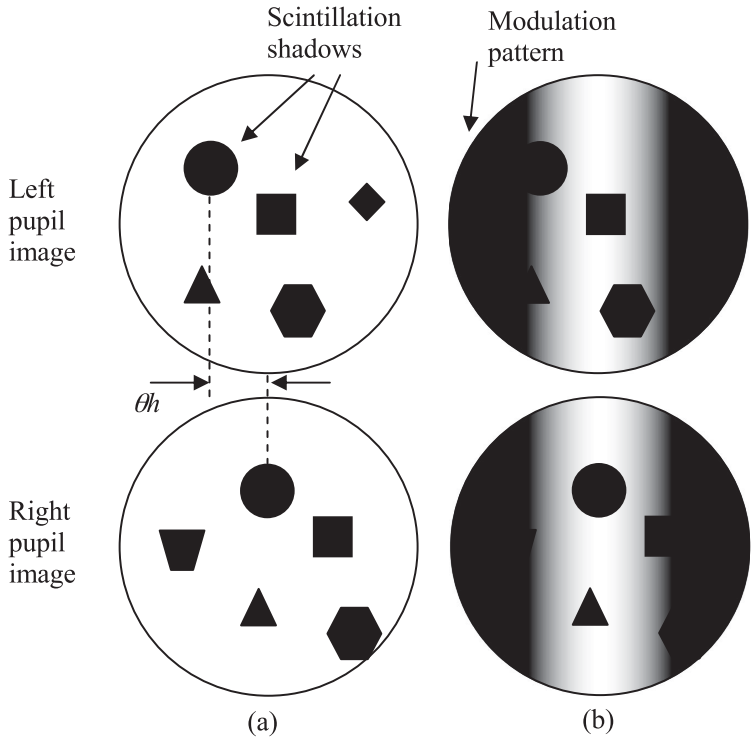

Figure 12. Schematic scintillation shadows (a) without and (b) with modulation.

separation between scintillation patterns is not small owing to large θ and/or large h, the correlation between modulated scintillation patterns will decrease.

In severe seeing conditions such that several speckles pass through a small FS, our solar SCIDAR technique loses sensitivity to scintillation caused by higher-layer turbulence.

6 CONCLUSIONS

We derived the formula for our solar SCIDAR method under the assumptions of a uniform intensity distribution and sparse speckle distributions. We realized that the cross-correlation of scintillation shadows yields peaks at positions corresponding to layer heights, although the shapes of peaks are blurred by both an extended seeing disc and a finite-sized FS. The effect of the blur is larger if the turbulent layer yielding the correlation peak is higher. In addition, the assumption of a sparse speckle distribution may be not valid, in particular under severe seeing conditions. In that case, the correlation between scintillation shadows deteriorates, especially when they arise from high turbulent layers. We thus consider that our present SCIDAR technique has a lower sensitivity when there is turbulence in higher layers.

The knife-edge effect caused by FSs yields a variety of peaks at the centre of the correlation plane, which interferes with the detection of SCI-peaks close to the centre. However, if the present solar SCIDAR technique is used for probing higher-layer turbulence, the knife-edge peak is less important because it always appears at the origin.

All the above-mentioned undesirable matters are relaxed as wavefront phase errors on the pupil plane decrease: small phase errors result in few speckles on the image plane, and then the sparse speckle assumption tends to be valid. Furthermore, shadows caused by the knife-edge effect are fainter because they reflect the bumps of phase errors. Therefore, better results can be expected if we use a high-performance pupil-plane AO system. Although we used our AO system in our SCIDAR observations, improvements in results by use of AO were not notable because of poor seeing conditions. In the Hida Observatory, a new full-scale AO system is under construction (Miura et al. 2012). By using the new AO system in SCIDAR observations, information on higher-layer turbulences will be obtained.

We applied our solar SCIDAR technique to the 60-cm domeless solar telescope of the Hida Observatory, Japan. We confirmed that scintillation peaks appeared on the correlation plane in various observational conditions. Therefore, we believe that our solar SCIDAR is able to measure the heights of turbulent layers. From observational results, we found that strong turbulent layers existed at 1–3 km height over the Hida Observatory. By repeating such observations over the seasons, we will obtain useful information for designing a MCAO system.

ACKNOWLEDGEMENTS

We thank J. Vernin for his valuable comments. This work was partly supported by a Grant-in-Aid for Scientific Research from the Ministry of Education, Culture, Sports, Science and Technology of Japan (No. 22244013, P.I. K. Ichimoto) and a Grant-in-Aid for Scientific Research (B) from the Japan Society for the Promotion of Science (No. 22340038).

REFERENCES

Avila R., Vernin J., Masciadri E., 1997, Appl. Opt., 36, 7898
Avila R., Vernin J., Sánchez L. J., 2001, A&A, 369, 364
Beckers J. M., 2001, Exp. Astron., 12, 1
Beckers J. M., Mason J., 1998, Proc. SPIE, 3352, 858
Beckers J. M., Rimmele T. R., 2004, Proc. SPIE, 5171, 195
Beckers J. M., Leon E., Mason J., Wilkins L., 1997, Solar Phys., 176, 23
Beran M. J., Whitman A. M., 1988, Appl. Opt., 27, 2178
Dainty J. C., 1975, in Dainty J. C., ed., Laser Speckle and Related Phenomena, Topics in Applied Optics 9. Springer-Verlag, Berlin, p. 255
Garnier D., 2007, PhD thesis, Natl. Univ. of Ireland, Galway
Horikawa H., Baba N., Ohtsubo M., Norimoto Y., Nishimura T., Miura N., 2004, Appl. Opt., 43, 3097
Kawate T., Hanaoka Y., Ichimoto K., Miura N., 2011, MNRAS, 416, 2154
Klückers V. A., Wooder N. J., Nicholls T. W., Adcock M. J., Munro I., Dainty J. C., 1998, A&AS, 130, 141
Labeyrie A., 1970, A&A, 6, 85
Langlois M., Moretto G., Richards K., Hegwer S., Rimmele T., 2004, Proc. SPIE, 5490, 59
Miura N., Kobayashi T., Sakuma S., Kuwamura S., Baba N., Hanaoka Y., Ueno S., Kitai R., 2006, Opt. Rev., 13, 338
Miura N., Kobayashi T., Sakuma S., Kuwamura S., Baba N., Hanaoka Y., Ueno S., Kitai R., 2007, Opt. Rev., 14, 159
Miura N. et al., 2009, Opt. Rev., 16, 558
Miura N. et al., 2011, Imaging and Applied Optics Technical Digest. OSA, Toronto, JWA26
Miura N. et al., 2012, Proc. SPIE, 8447, 8447
Rimmele T. R., 2000, Proc. SPIE, 4007, 218
Rocca A., Roddier F., Vernin J., 1974, JOSA, 64, 1000
Roddier F., 1981, in Wolf E., ed., Progress in Optics. North-Holland, Amsterdam, p. 283
Schmidt D., Berkefeld T., Heidecke F., von der Lühe O., Soltau D., 2009, Proc. SPIE, 7439, 74390X
Weiß A. R., Hippler S., Kasper M. E., Feldt M., 2002, Proc. SPIE, 4538, 135

APPENDIX A: DERIVATION OF EQUATION (19)

Substituting equation (16) into (18), we obtain

$$I(\boldsymbol{r};\boldsymbol{w}_a) = p(\boldsymbol{r}) \cdot \sum_{m=1}^{M} \int_{Area[Q]} \mathrm{d}\boldsymbol{w}'\, s^2\left(\boldsymbol{r} - \frac{h}{f}\left[\boldsymbol{w}_a + \boldsymbol{w}' - \boldsymbol{w}_m\right]\right) |c_m|^2 . \tag{A1}$$

By considering

$$s^2\left(\boldsymbol{r} - \frac{h}{f}\left[\boldsymbol{w}_a + \boldsymbol{w}' - \boldsymbol{w}_m\right]\right) = s^2\left(\boldsymbol{r} - \frac{h}{f}\left[\boldsymbol{w}_a - \boldsymbol{w}_m\right]\right) * \delta\left(\boldsymbol{r} - \frac{h}{f}\boldsymbol{w}'\right), \tag{A2}$$

equation (A1) can be rewritten as

$$\begin{aligned} I(\boldsymbol{r};\boldsymbol{w}_a) &= p(\boldsymbol{r})\left\{\sum_{m=1}^{M}\left[s^2\left(\boldsymbol{r} - \frac{h}{f}\left[\boldsymbol{w}_a - \boldsymbol{w}_m\right]\right)|c_m|^2\right] * \int_{Area[Q]} \delta\left(\boldsymbol{r} - \frac{h}{f}\boldsymbol{w}'\right)\mathrm{d}\boldsymbol{w}'\right\} \\ &= p(\boldsymbol{r})\left\{\sum_{m=1}^{M}\left[s^2\left(\boldsymbol{r} - \frac{h}{f}\left[\boldsymbol{w}_a - \boldsymbol{w}_m\right]\right)|c_m|^2\right] * Q\left(\frac{f}{h}\boldsymbol{r}\right)\right\}. \end{aligned} \tag{A3}$$

Using

$$s^2\left(\boldsymbol{r} - \frac{h}{f}\left[\boldsymbol{w}_a - \boldsymbol{w}_m\right]\right) = \left|\psi_0\left(\boldsymbol{r} - \frac{h}{f}\boldsymbol{w}_a\right)\right|^2 * \delta\left(\boldsymbol{r} + \frac{h}{f}\boldsymbol{w}_m\right), \tag{A4}$$

the summation in equation (A3) leads to

$$\sum_{m=1}^{M}\left[s^2\left(\boldsymbol{r} - \frac{h}{f}\left[\boldsymbol{w}_a - \boldsymbol{w}_m\right]\right)|c_m|^2\right] = \left|\psi_0\left(\boldsymbol{r} - \frac{h}{f}\boldsymbol{w}_a\right)\right|^2 * \sum_{m=1}^{M}|c_m|^2\,\delta\left(\boldsymbol{r} + \frac{h}{f}\boldsymbol{w}_m\right). \tag{A5}$$

The second term on the right-hand side becomes, using equation (9),

$$\sum_{m=1}^{M}|c_m|^2\,\delta\left(\boldsymbol{r} + \frac{h}{f}\boldsymbol{w}_m\right) = T\left(-\frac{f}{h}\boldsymbol{r}\right). \tag{A6}$$

Substituting equations (A5) and (A6) into (A3), we finally obtain equation (19).

This paper has been typeset from a TEX/LATEX file prepared by the author.